Computational Design of Virus-Like Protein Assemblies on Carbon Nanotube Surfaces

Gevorg Grigoryan, *et al.*

Science **332**, 1071 (2011);
DOI: 10.1126/science.1198841

contrasts at each of the high-temperature transitions (i.e., spinel ↔ garnet+magnesiowüstite ↔ perovskite+magnesiowüstite), the value of $\Gamma_{p\text{-}gt}$, and composition, post-garnet transitions may facilitate the formation of secondary upwellings and thus contribute to the elevated upper-mantle temperatures in region III, a positive geoid anomaly, and, perhaps, the richness of bathymetric features away from seamount chains. Finally, any temporary ponding of lower-mantle flow at *660* suggests that pipe flow or zonation of mantle plumes (*7*, *39*–*41*) must be shallow-mantle phenomena, and that isotope signatures of surface lavas cannot be used to map geochemical domains in the lower mantle.

References and Notes

1. J. T. Wilson, *Can. J. Phys.* **42**, 893 (1963).
2. W. J. Morgan, *Nature* **230**, 42 (1971).
3. G. F. Davies, *J. Geophys. Res.* **93**, 10467 (1988).
4. N. H. Sleep, *J. Geophys. Res.* **95**, 6715 (1990).
5. V. Courtillot, A. Davaille, J. Besse, J. Stock, *Earth Planet. Sci. Lett.* **205**, 295 (2003).
6. S. R. Hart, E. H. Hauri, L. A. Oschmann, J. A. Whitehead, *Science* **256**, 517 (1992).
7. D. Hanano, D. Weis, J. S. Scoates, S. Aciego, D. J. DePaolo, *Geochem. Geophys. Geosyst.* **11**, Q01004 (2010).
8. N. M. Ribe, U. R. Christensen, *Earth Planet. Sci. Lett.* **171**, 517 (1999).
9. B. Steinberger, R. J. O'Connell, *Geophys. J. Int.* **132**, 412 (1998).
10. J. Tarduno, H.-P. Bunge, N. Sleep, U. Hansen, *Science* **324**, 50 (2009).
11. C. J. Allègre, *Philos. Trans. R. Soc. Lond. A* **360**, 2411 (2002).
12. D. L. Anderson, *Geophys. Res. Lett.* **27**, 3623 (2000).
13. S. P. Grand, *Philos. Trans. R. Soc. Lond. A* **360**, 2475 (2002).
14. C. Li, R. D. van der Hilst, E. R. Engdahl, S. Burdick, *Geochem. Geophys. Geosyst.* **9**, Q05018 (2008).
15. R. Montelli *et al.*, *Science* **303**, 338 (2004).
16. C. J. Wolfe *et al.*, *Science* **326**, 1388 (2009).
17. C. J. Wolfe *et al.*, *Earth Planet. Sci. Lett.* **303**, 267 (2011).
18. G. Helffrich, *Rev. Geophys.* **38**, 141 (2000).
19. T. Katsura, E. Ito, *J. Geophys. Res.* **94**, 15663 (1989).
20. X. Li *et al.*, *Nature* **405**, 938 (2000).
21. J. A. Collins, F. L. Vernon, J. A. Orcutt, R. A. Stephen, *Geophys. Res. Lett.* **29**, 1522 (2002).
22. I. Wölbern *et al.*, *Geophys. J. Int.* **166**, 767 (2006).
23. Y. Shen, C. J. Wolfe, S. C. Solomon, *Earth Planet. Sci. Lett.* **214**, 143 (2003).
24. A. Deuss, S. A. T. Redfern, K. Chambers, J. H. Woodhouse, *Science* **311**, 198 (2006).
25. J. Lawrence, P. M. Shearer, *Geophys. J. Int.* **174**, 143 (2008).
26. A. Deuss, *Surv. Geophys.* **30**, 301 (2009).
27. C. Houser, Q. Williams, *Earth Planet. Sci. Lett.* **296**, 255 (2010).
28. N. Schmerr, E. Garnero, A. McNamara, *Earth Planet. Sci. Lett.* **294**, 143 (2010).
29. Materials and Methods are available on *Science* Online.
30. Q. Cao, P. Wang, R. D. van der Hilst, M. V. de Hoop, S.-H. Shim, *Phys. Earth Planet. Inter.* **180**, 80 (2010).
31. H. Morishima *et al.*, *Science* **265**, 1202 (1994).
32. The Clapeyron slope of the wadsleyite to ringwoodite transition is positive (*42*) but not well constrained experimentally.
33. T. Irifune *et al.*, *Science* **279**, 1698 (1998).
34. D. J. Weidner, Y. Wang, *J. Geophys. Res.* **103**, (B4), 7431 (1998).
35. K. Hirose, *J. Geophys. Res.* **107**, (B4), 2078 (2002).
36. N. Nishiyama, T. Yagi, *J. Geophys. Res.* **108**, 2255 (2003).
37. M. Akaogi, E. Ito, *Phys. Earth Planet. Inter.* **114**, 129 (1999).
38. L. Cserepes, D. A. Yuen, *Earth Planet. Sci. Lett.* **183**, 61 (2000).
39. D. J. DePaolo, E. M. Stolper, *J. Geophys. Res.* **101**, (B5), 11643 (1996).
40. J. Blichert-Toft, F. Albarède, *Earth Planet. Sci. Lett.* **282**, 190 (2009).
41. C. G. Farnetani, A. W. Hofmann, *Earth Planet. Sci. Lett.* **282**, 314 (2009).
42. A. Suzuki *et al.*, *Geophys. Res. Lett.* **27**, 803 (2000).

Acknowledgments: This research was supported by the CSEDI (Collaborative Studies of Earth's Deep Interior, grant EAR-0757871) and CMG (Collaborative Mathematical Geosciences, grant DMS-0724778) programs of the U.S. National Science Foundation and a Shell research fellowship awarded to Q.C. The seismic waveforms used here were all retrieved from the Data Management Center of IRIS (Incorporated Research Institutions for Seismology).

Supporting Online Material

www.sciencemag.org/cgi/content/full/332/6033/1068/DC1
Materials and Methods
SOM Text
Figs. S1 to S11
References (*43*, *44*)

11 January 2011; accepted 21 April 2011
10.1126/science.1202731

Computational Design of Virus-Like Protein Assemblies on Carbon Nanotube Surfaces

Gevorg Grigoryan,[1]* Yong Ho Kim,[2]* Rudresh Acharya,[1] Kevin Axelrod,[3] Rishabh M. Jain,[3] Lauren Willis,[3] Marija Drndic,[3] James M. Kikkawa,[3] William F. DeGrado[1,2]†

There is a general need for the engineering of protein-like molecules that organize into geometrically specific superstructures on molecular surfaces, directing further functionalization to create richly textured, multilayered assemblies. Here we describe a computational approach whereby the surface properties and symmetry of a targeted surface define the sequence and superstructure of surface-organizing peptides. Computational design proceeds in a series of steps that encode both surface recognition and favorable intersubunit packing interactions. This procedure is exemplified in the design of peptides that assemble into a tubular structure surrounding single-walled carbon nanotubes (SWNTs). The geometrically defined, virus-like coating created by these peptides converts the smooth surfaces of SWNTs into highly textured assemblies with long-scale order, capable of directing the assembly of gold nanoparticles into helical arrays along the SWNT axis.

De novo protein design has historically been used to test the principles governing protein folding and assembly (*1*–*3*). These principles have also been extended to the design of structures capable of binding metal ions (*4*, *5*), peptides (*6*–*8*), DNA (*9*, *10*), inorganic materials (*11*), and proteins that catalyze reactions similar to those found in nature (*12*–*15*). However, protein design might have greater impact when applied to the engineering of controllable, structurally defined molecular assemblies (*16*). A solution to this problem would enable the manipulation and organization of objects on the molecular and atomic levels, a major challenge of modern nanoscience.

We describe a general approach for designing molecules that assemble along geometrically specific surfaces into a predefined superstructure. Earlier studies focused on amphiphilic peptides that encourage binding and assembly at soft interfaces (*17*–*19*), but without explicit consideration of interpeptide packing geometry that defines the nano- to macrostructure of the overall complex. A good design strategy for encoding a specific mode of assembly is to engineer a protein structural unit that presents functional groups compatible with the targeted surface and associates into a periodic superstructure with a geometric repeat matching that of the targeted substrate (Fig. 1A). However, an infinite continuum of such symmetry-matching arrangements can be generated out of common protein structural units. Thus, the most challenging aspect of designing such a surface-organizing assembly is the identification of a reasonable superstructure geometry, a problem we address in this study. Here, we apply our approach to design peptides that wrap single-walled carbon nanotubes (SWNTs) in a structurally specific manner, creating a richly textured molecular surface. Previously studied biomolecules that interact with SWNTs include single-stranded DNA molecules (*20*, *21*), nanotube-binding peptides selected by phage-display (*22*), and synthetic peptides with chemical features that favor SWNT binding (*23*, *24*). Beyond interacting with and solubilizing SWNTs, a unique and relatively unexplored potential offered by biomolecules is the ability to program structurally specific modes of surface assembly, enabling

[1]Department of Biochemistry and Biophysics, University of Pennsylvania, Philadelphia, PA 19104, USA. [2]Department of Chemistry, University of Pennsylvania, Philadelphia, PA 19104, USA. [3]Department of Physics and Astronomy, University of Pennsylvania, Philadelphia, PA 19104, USA.

*These authors contributed equally to this work.
†To whom correspondence should be addressed. E-mail: wdegrado@mail.med.upenn.edu

nucleation of further superstructure, functionalization, and manipulation (*25*).

Our design process consists of three selection rules, which successively restrict the space of possible peptide-surface assemblies and ultimately dictate peptide sequence (Fig. 1). Selection rule one identifies groups compatible with the target surface, as well as a protein structural unit capable of displaying such groups in a productive manner (Fig. 1B). Selection rule two defines the intersubunit packing of these units on the target surface. Symmetry operations are used to create an elementary unit cell, which is then replicated to match the geometric repeat of the surface (Fig. 1C). A continuum of assemblies remains possible at this point, each creating new protein-protein interfaces, within the unit cell and between neighboring unit cells. The key insight is provided by selection rule three, which ensures that these interfaces are designable—that is, they can be accommodated in a stable and specific manner (Fig. 1D). Designable protein structural motifs occur frequently in nature, such that a structural database search can be used to assess the feasibility of specific intersubunit packing in addition to revealing sequence features that encode it (*26*). In summary, the three selection rules define the intrinsic recognition motif, and its packing into a higher-order assembly in accord with the long-range order of the underlying surface.

These selection rules emerged from our efforts to engineer peptides targeting common species of SWNTs. In picking a functional group for contacting the SWNT (selection rule one), we avoided strong hydrophobic recognition motifs employed in earlier studies (*23*), instead relying on weaker protein-SWNT interactions to encourage the cooperative formation of the intended higher-order assembly (Fig. 1A). We therefore chose the C_α methylene of Gly or the C_β methyl of Ala, presented in a repeating manner on an α helix as the elementary structural unit.

Selection rule two stipulates that the arrangement of protein structural units should match the symmetry of the underlying surface. The cylindrical shape of a SWNT suggested an assembly with rotational or rotational-screw symmetry, so we considered α-helical coiled coils forming a supercoil along the SWNT axis (Fig. 1E). Common SWNTs have relatively hydrophobic surfaces and radii in the range of ~3.75 to 4.1 Å [for the (5,6), (5,7), and (3,8) chiralities]. This, together with the choice of a small side chain for surface recognition, defined the radius of the coiled coil to be ~9 Å, restricting the stoichiometry of the bundle to between five and seven units (*26*). We chose an antiparallel hexamer over a parallel α-helical bundle to exploit the additional degree of freedom (axial shift) available to antiparallel interfaces (*26*). Although SWNTs are relatively smooth, their electronic surface is not entirely homogeneous, and we considered that it may be advantageous in design to match the pitch angle of the helices formed by overlapping benzenoid rings down SWNT surfaces (Fig. 1E) (*27*).

Although the first two selection rules identified a specific topology, a large number of possible bundles with reasonable interfaces could be generated based on the four remaining parameters: (i) the inter-helical separation, (ii) starting helical phase, (iii) superhelical pitch, and (iv) helical axial shift. Allowing 50 discrete values for each parameter within geometrically feasible ranges results in 6,250,000 possible design templates. We had previously found that no more than 1 in 100 α-helical coiled coils constructed using geometrically feasible parameter values are, in fact, designable with natural amino acids (*26*). Therefore, in selection rule three, we searched for assembly parameters that optimized the designability of the modeled interfaces, leading to a single most designable template for each targeted SWNT.

To assess designability, we used a rapid distance-matrix–based method for searching tertiary motifs in the Protein Data Bank (PDB) that are geometrically similar to the query interface (Fig. 2A). The number of matches within a given cutoff of the query interface amounts to a metric of its designability, and sequences of the matches help

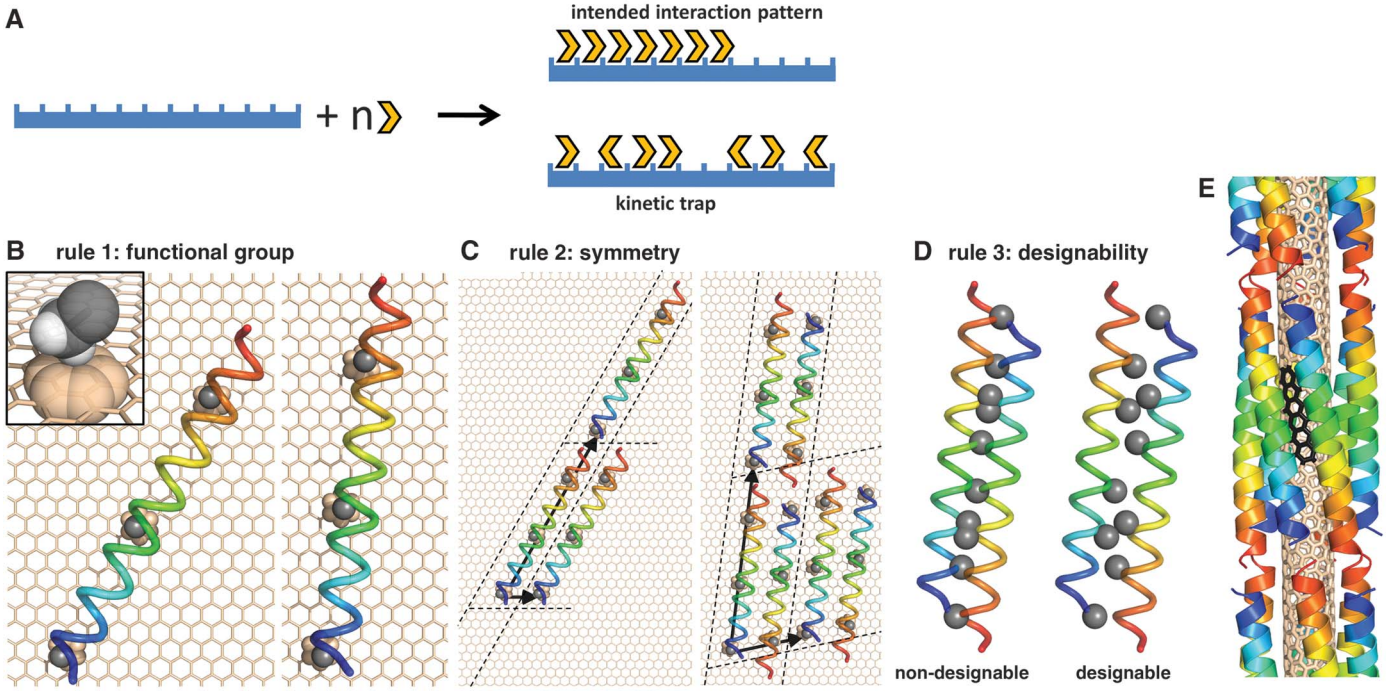

Fig. 1. (**A**) Simplified diagram of the surface assembly process (*34*). The design goal is to achieve ordered arrays of peptide subunits on the target surface (global order; top outcome in the figure) and to avoid kinetic traps of surface binding (local order; bottom outcome), which can be caused by overly strong interactions between individual subunits and the surface. (**B** to **D**) The general design framework is illustrated on the example of decorating a graphene sheet. (B) Selection rule one: C_β methyl group of Ala and the α helix are picked as the surface-contacting functional group and structural unit, respectively. (C) Selection rule two: Two possible unit cells, a single helix and an antiparallel dimer, are shown along with the corresponding Bravais-lattice vectors defining unit-cell images. (D) Assemblies containing undesignable interfaces are discarded in selection rule three (differences in designability are usually much more subtle than illustrated here for clarity). (**E**) Optimal template geometry designed to target the (3,8) SWNT surface (the array of adjacent benzenoid rings in black illustrates the helical pattern of the SWNT).

define features encoding intersubunit packing. Because this information is gathered from a wide range of structural contexts, sequences of the matches should be highly divergent at all positions except those that are particularly critical to the stability and structural specificity of the motif. The conserved positions are held constant in design, whereas the variable positions provide handles for encoding additional features, such as interaction with SWNTs; modulation of solubility, stability, and specificity; or recruitment of additional functionality.

The selection rules were implemented into an automated procedure and applied to the design of assemblies on the surfaces of SWNTs (3,8), (5,7), and (5,6), matching both size and pitch angle to each SWNT [corresponding pitch angles were –14.7°, –5.5°, and –3°, respectively (*27*)]. An antiparallel hexamer has two geometrically distinct helix-helix interfaces (Fig. 2A, inset). The designability of these interfaces in the optimal template was starkly different among the three pitch angles (Fig. 2, A and B). For example, the optimal –14.7° template identified 119 and 89 natural motifs that were within 0.6 Å C_α root mean square deviation (RMSD) of the two helix-helix interfaces making up this assembly. The corresponding values for the best –5.5° structure were 4 and 7, and none were found within this cutoff for the –3° structure. Thus, the –14.7° template would be considered a much more designable target using common, genetically encoded amino acids.

Profiles of residue propensities in aligned sequences (Fig. 2C) show that optimal designability is reached when the two unique interfaces of the hexamer are quite different: One should be a "tight" Ala coil-like interface, whereas the other should resemble an antiparallel Leu zipper-like motif. Note that this information is obtained automatically, without resorting to extensive side-chain repacking calculations on candidate backbone structures.

Having chosen the –14.7° structure as the target, we followed two paths to complete the design process. In the first, a sequence was computationally optimized to adopt this hexameric antiparallel bundle around the (3,8) SWNT, constraining the strongly conserved positions from propensity profiles (positions "d" and "e"; Fig. 2C). Standard computational design techniques were applied to select the remaining variable positions [section 1.2 in the supporting online material (*27*)] producing two sequences, HexCoil-Gly and HexCoil-Ala (Fig. 3A), differing only in the identity of the SWNT-contacting position (Gly or Ala, respectively).

In a second approach, we sought a preassembled scaffold from within the PDB that would be geometrically compatible with wrapping a SWNT and amenable to further design. Our designability analysis revealed a bundle remarkably similar to our –14.7° template (0.9 Å C_α RMSD over 156 residues) in the inner ring of helices of a domain-swapped helical protein (called DSD; PDB code 1G6U) (Fig. 3E and figs. S4 and S5) (*28*). Additionally, the strong sequence features discovered for the (3,8)-optimal template (Fig. 2C) were also present in DSD. Therefore, the central pore-lining Glu and Lys residues of DSD were converted to Gly or Ala to accommodate a SWNT, resulting in peptides designated DSD-Gly and DSD-Ala.

The hierarchic principles of our design approach suggest that a large portion of the driving force for assembly should originate from modestly

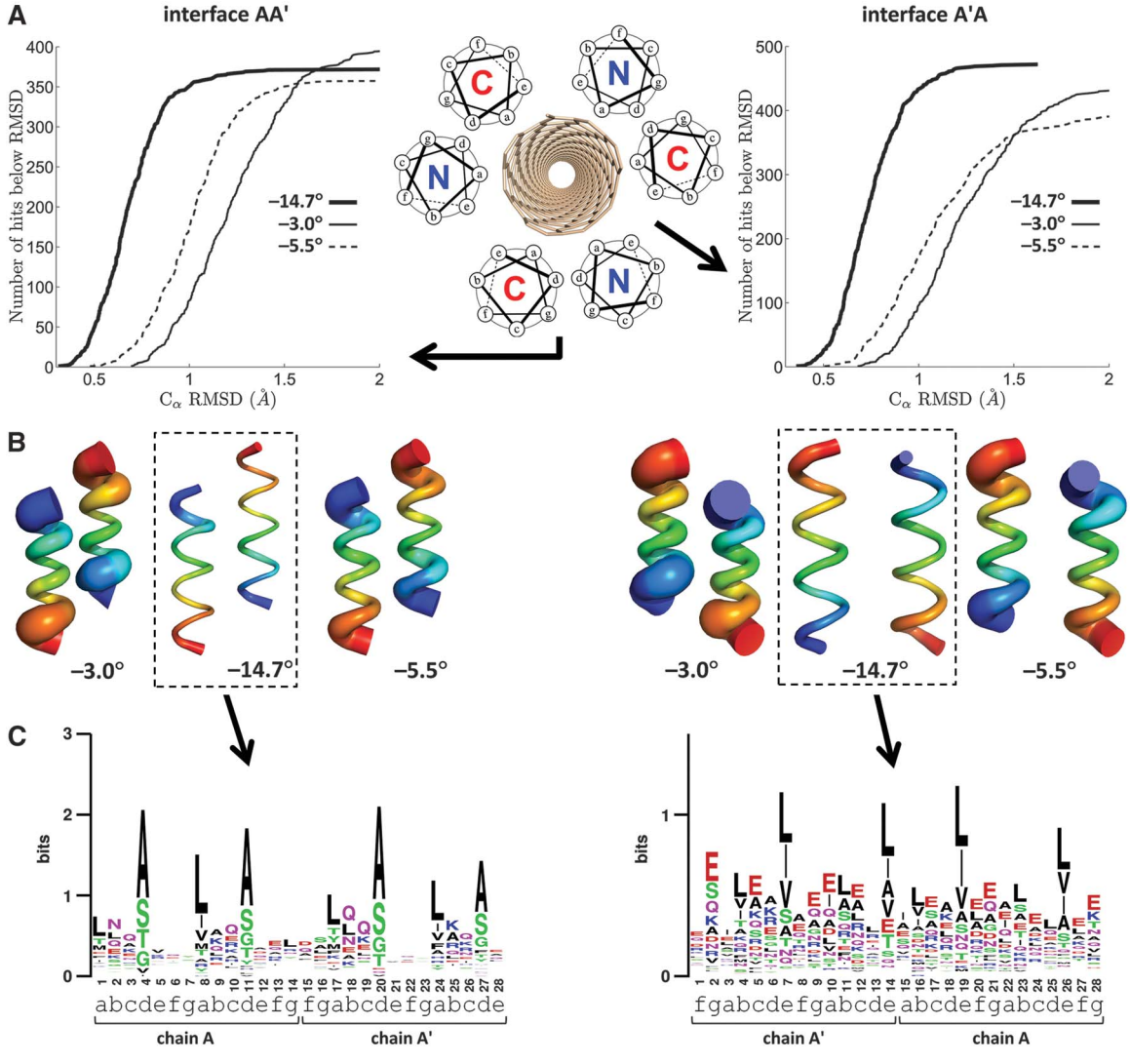

Fig. 2. Designability analysis in selection rule three. The two unique interfaces of an antiparallel homohexamer are designated here as AA′ and A′A and illustrated in the left and right columns, respectively. (**A**) Number of matches as a function of the C_α RMSD cutoff. (**B**) Structural variation in the top 100 best matches. Tube thickness is equal to the mean square deviation of the corresponding atom within the ensemble of top 100 matches. The blue-to-red coloring indicates the N-to-C terminal direction. (**C**) Sequence logo diagrams for the two interfaces of the (3,8)-targeted template derived from unique matches with C_α RMSD below 0.5 and 0.6 Å for AA′ and A′A, respectively (*35*). Heptad assignments, in the context of the full hexamer, are indicated for each sequence position.

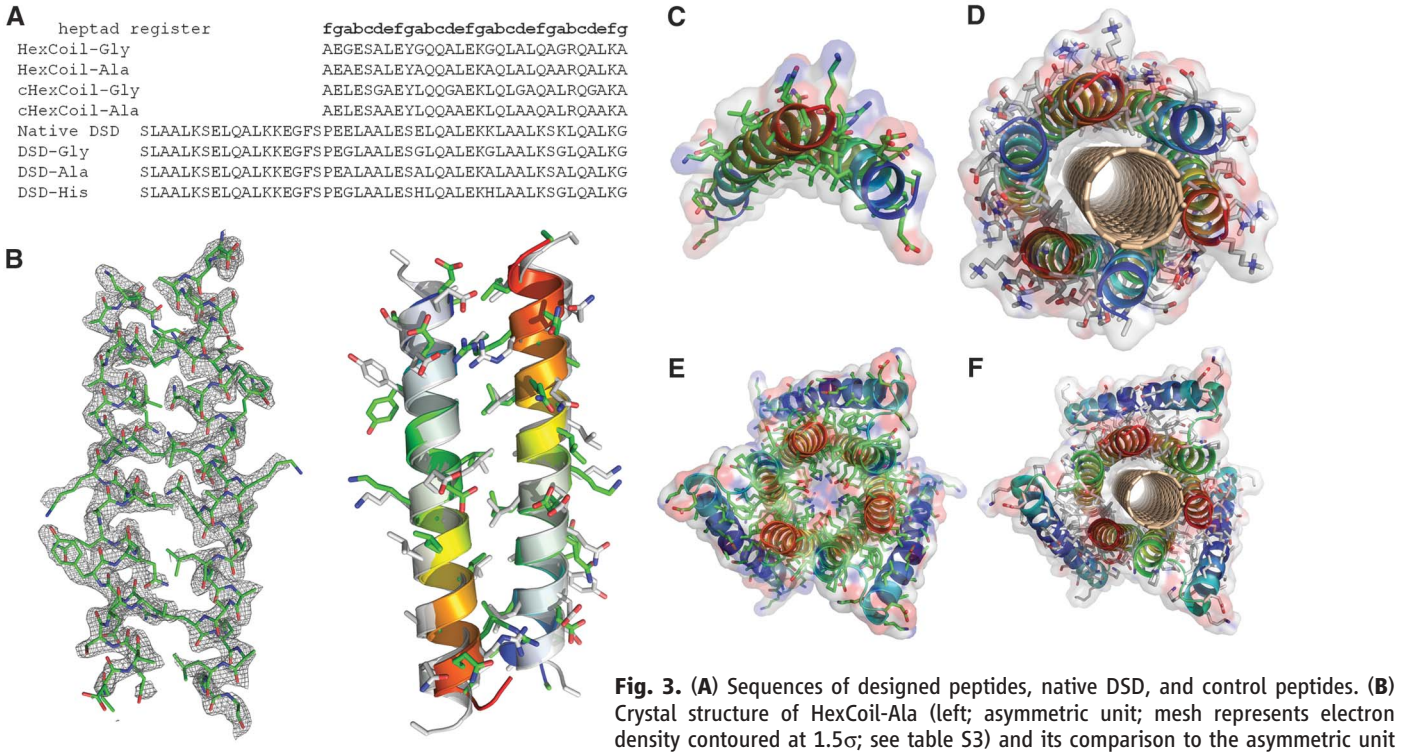

Fig. 3. (**A**) Sequences of designed peptides, native DSD, and control peptides. (**B**) Crystal structure of HexCoil-Ala (left; asymmetric unit; mesh represents electron density contoured at 1.5σ; see table S3) and its comparison to the asymmetric unit of the designed oligomer (right; gray structures correspond to the design). (**C**) The Ala-rich surface of the asymmetric unit of the HexCoil-Ala crystal structure is well poised to interact with a SWNT. (**D**) Model structure of HexCoil-Gly with a (3,8) SWNT. Blue-to-red coloring indicates the N-to-C terminal direction. (**E**) Crystal structure of native DSD. (**F**) Model of DSD-Ala with a (3,8) SWNT. Van der Waals surfaces are shown semitransparently in (C) to (F).

favorable helix-helix interactions, which should stabilize the basic antiparallel dimeric unit, even in the absence of SWNTs. Without the underlying solid substrate, the hexameric bundle structure might not be the most stable one formed, but we expected to see assembly into related bundles in which the dimeric interface was preserved. Indeed, sedimentation equilibrium analytical ultracentrifugation showed DSD-Gly and DSD-Ala to exist in a dimer-hexamer equilibrium between 10 and 100 μM peptide concentration (fig. S7). HexCoil-Ala associated into tetramers (fig. S8), whose structure was solved using diffraction data extending to 2.44 Å resolution by x-ray crystallography (Fig. 3, B and C; PDB accession code 3S0R). The asymmetric unit consists of an antiparallel dimer, whose structure is within 1.2 Å of the designed model (calculated over the backbone of 20 central residues per monomer). The designed Ala-rich face is well-situated to interact with the surface of the SWNT (Fig. 3C). Finally, far ultraviolet circular dichroism spectroscopy of these peptides confirmed their helical content in solution and when bound to SWNT (fig. S9). HexCoil-Gly, which contains multiple helix-destabilizing Gly residues, assembled only in the presence of SWNTs (fig. S9), showing surface-induced folding similar to previously designed surface-binding peptides (*29*, *30*).

The peptides formed water-soluble assemblies of SWNTs, producing aqueous suspensions that were stable for months. Two-dimensional photoluminescence (2D-PL) spectra were used to identify individual SWNT chiralities through their characteristic resonances (*31*) and to rule out aggregation of SWNTs, which induces energy transfer between different species (*32*). Designed peptides produce SWNT suspensions with 2D-PL peaks corresponding to (5,6), (5,7), and (3,8) chiralities (Fig. 4, A to C). The de novo designed peptides HexCoil-Ala and HexCoil-Gly sequester significantly more SWNTs into solution, compared with DSD variants (Fig. 4B). Interestingly, though the (3,8) species is a minor product in the mixture of SWNTs used in our experiments, HexCoil-Ala and HexCoil-Gly show a dominant peak corresponding to this chirality (Fig. 4, B and C). This is of particular importance given that the target substrate for these designs was indeed the (3,8)-species SWNT.

A number of control peptides were prepared to evaluate the structural mode of SWNT/peptide assembly. To probe the role of the small Ala and Gly residues contacting the SWNT, native DSD and an analog of DSD-Gly with two of its Gly residues changed to His were studied. Furthermore, to test the role of helix-helix packing in HexCoil-Gly and HexCoil-Ala, the apolar residues at the "d" and "e" positions that pack at the two distinct helix-packing interfaces and the SWNT-contacting "a" position were interchanged (fig. S12). The resulting peptides, cHexCoil-Gly and cHexCoil-Ala (Fig. 3A), have identical amino acid compositions, hydrophobicity, and helical faces, and nearly identical hydrophobic moments (a measure of amphiphilicity) as their parents, but differ in their abilities to engage in the detailed packing interactions intended to stabilize surface assemblies. These negative control peptides (native DSD, DSD-His, cHexCoil-Gly, or cHexCoil-Ala) were very inefficient at solubilizing SWNTs (Fig. 4A and fig. S12), verifying the intended mode of SWNT contact and suggesting that the success of our designs rests on the ability to form favorable intersubunit interactions and a higher-order assembly.

Once SWNTs are wrapped by peptides in a structurally determined way, their solvent-exposed surfaces can be further elaborated to direct the assembly, or even the synthesis, of a third biological or nonbiological layer. To illustrate this, we used the peptide/SWNT assembly to direct nucleation and assembly of gold nanoclusters in a geometrically defined manner. The DSD-Gly peptide appeared advantageous for these studies, as its peripheral helices packing against the central hexameric ring allow for the construction of independent outward-facing binding sites along a larger-radius superhelix, facilitating microscopic imaging. A single Cys was introduced near the N terminus of DSD-Gly, such that pairs of symmetry-related helices created convergent gold-binding sites (Fig. 4G and fig. S11). Addition of Au(III) under reducing conditions led to the appearance of 2- to 4-nm gold clusters visible by transmission electron microscopy (TEM) (Fig. 4 and fig. S3). Consistent with the design model, the pattern of spots is linear and systematically in-phase, and the observed interparticle spacing of 47 Å is

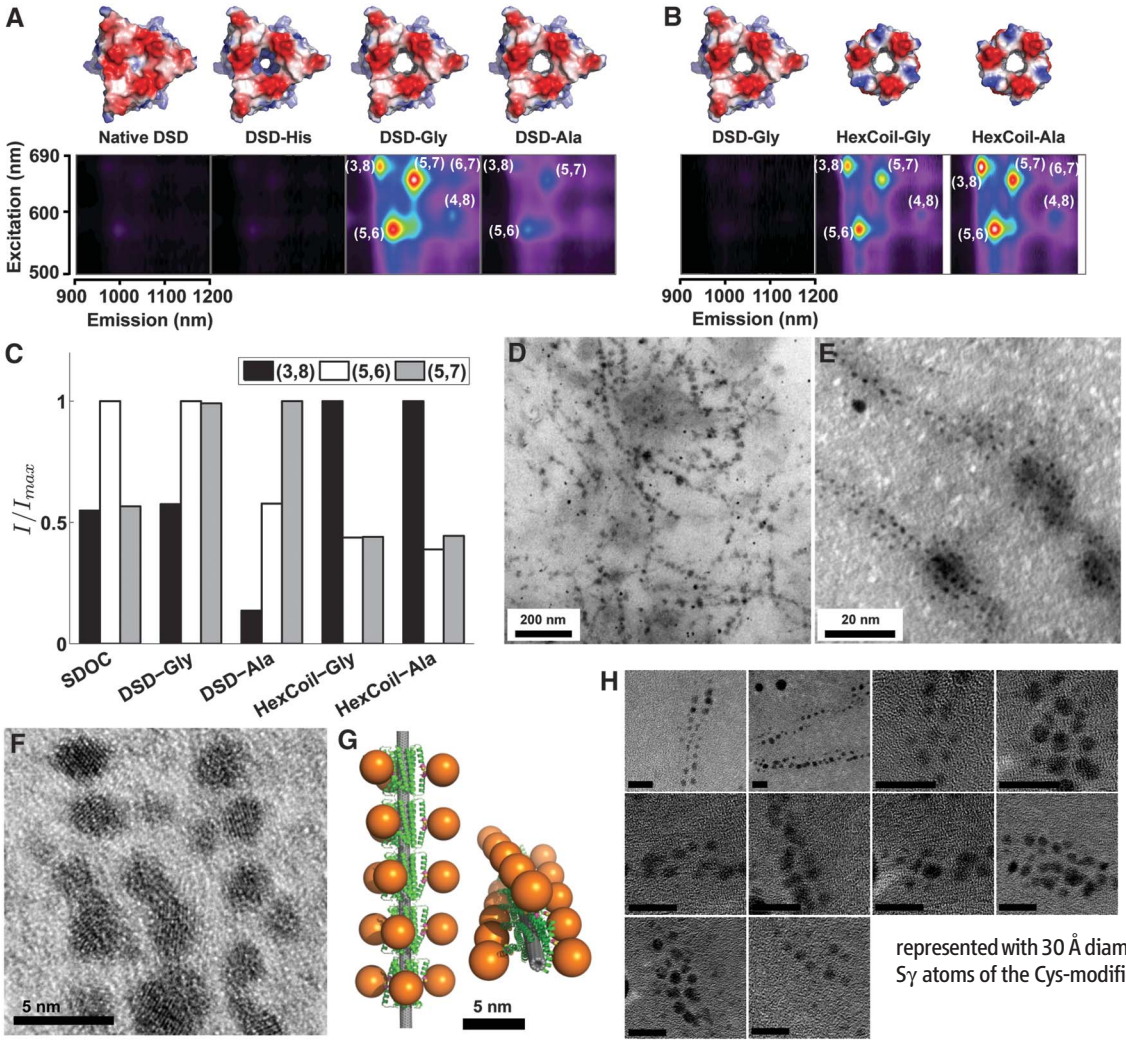

Fig. 4. 2D-PL and TEM analysis of SWNT/peptide complexes. (**A** and **B**) 2D-PL spectra of SWNT suspensions produced by (A) DSD-based peptides and (B) de novo designed peptides (pseudocolor scale is internally consistent within each section). (**C**) Fitting photoluminescence maps to a sum of 2D Lorentzians provides the total intensity weight contribution of each SWNT species, *I*. Shown are relative contributions of the three most contributing SWNT types in suspensions produced by four peptides and, for reference, the common surfactant sodium deoxy cholate (SDOC) (spectrum in fig. S14). In each case, weights are normalized to the most contributing species. (**D** to **F** and **H**) TEM images of gold nanoparticles grown on Cys-modified DSD-Gly hexamers wrapped around individual SWNTs. Panel (E) is a higher magnification version of (D), and panel (F) contains a high-resolution TEM image. Scale bars are 10 nm in (H). (**G**) Computational model of the complex. Gold particles are represented with 30 Å diameter spheres attached to the Cys Sγ atoms of the Cys-modified DSD-Gly.

in very good agreement with the model's prediction of 52 Å (figs. S1 to S3) (*27*).

The selection rules described here provide an objective reproducible method for designing surface-binding peptides. Their aim is to assure that all effects are favorable for the formation of the intended assembly. Optimal interaction geometry between protein units, physicochemical compatibility between the surface and the protein, and matching between the geometry of the assembly and the symmetry of the substrate are all encoded at the same time in a "minimally frustrated" design. In applying this strategy to SWNT surfaces, we expected that the dominant surface features would be the radius and the water-repellant nature; thus, the driving force for assembly would originate primarily from matching the size and hydrophobicity of the SWNT, as well as intersubunit packing. Indeed, this strategy worked. The intended SWNTs were bound, thereby converting the very short-scale periodicity of a SWNT surface to long-scale periodicity of a SWNT/protein assembly, as illustrated by using the complex to further direct the nucleation of an additional layer of gold nanoclusters.

SWNTs present a challenging case for organizing structurally specific assemblies because of their relatively featureless surfaces. Other molecular surfaces, such as ionic structures or boron nitride nanotubes (*33*), are likely to have much higher heterogeneity in presented atomic groups, leading to better potential for anisotropy with respect to surface interactions. In such cases, we would expect that the orientation of the coating assembly relative to the crystal lattice would be a very important discriminator and director of order. It is encouraging that even with the rather simple and smooth surfaces of SWNTs, we have already achieved a substantial level of success. The DSD versus HexCoil series of peptides illustrate different endpoints of the design process. Whereas the DSD scaffold was serendipitously discovered to approximately match the assembly geometry optimized via our approach, HexCoil-Ala and HexCoil-Gly were designed de novo to bind the (3,8) SWNT. Thus, it is encouraging that the latter peptides are more efficient and considerably more selective agents for solubilizing the desired target, showing a strong preference for solubilizing this tube type despite it being a minor component in a mixture of SWNTs. It is possible that the interfaces in the HexCoil peptides, which are unencumbered by the presence of a more involved tertiary packing, are sufficiently preorganized to allow selective binding, but not so rigid as to require a perfect fit for selective recognition to take place.

In summary, biological systems specialize in assembly, and hybrid nano-bio structures provide a powerful way to direct the assembly and tune the properties of nanomaterials. Computational protein design provides the means to do so in a highly directed and functionally relevant manner.

References and Notes

1. M. H. Cordes, A. R. Davidson, R. T. Sauer, *Curr. Opin. Struct. Biol.* **6**, 3 (1996).
2. B. I. Dahiyat, S. L. Mayo, *Science* **278**, 82 (1997).
3. B. Kuhlman *et al.*, *Science* **302**, 1364 (2003).
4. D. Ghosh, V. L. Pecoraro, *Curr. Opin. Chem. Biol.* **9**, 97 (2005).
5. J. R. Calhoun *et al.*, *Biopolymers* **80**, 264 (2005).
6. G. Ghirlanda, J. D. Lear, A. Lombardi, W. F. DeGrado, *J. Mol. Biol.* **281**, 379 (1998).
7. J. Reina *et al.*, *Nat. Struct. Biol.* **9**, 621 (2002).
8. G. Grigoryan, A. W. Reinke, A. E. Keating, *Nature* **458**, 859 (2009).
9. J. Ashworth *et al.*, *Nature* **441**, 656 (2006).

10. J. S. Kim, C. O. Pabo, *Proc. Natl. Acad. Sci. U.S.A.* **95**, 2812 (1998).
11. D. L. Masica, S. B. Schrier, E. A. Specht, J. J. Gray, *J. Am. Chem. Soc.* **132**, 12252 (2010).
12. D. Röthlisberger *et al.*, *Nature* **453**, 190 (2008).
13. L. Jiang *et al.*, *Science* **319**, 1387 (2008).
14. D. Häring, M. D. Distefano, *Bioconjug. Chem.* **12**, 385 (2001).
15. J. Kaplan, W. F. DeGrado, *Proc. Natl. Acad. Sci. U.S.A.* **101**, 11566 (2004).
16. R. Fairman, K. S. Akerfeldt, *Curr. Opin. Struct. Biol.* **15**, 453 (2005).
17. W. F. DeGrado, J. D. Lear, *J. Am. Chem. Soc.* **107**, 7684 (1985).
18. S. Segman, M. R. Lee, V. Vaiser, S. H. Gellman, H. Rapaport, *Angew. Chem. Int. Ed. Engl.* **49**, 716 (2010).
19. H. Rapaport, *Supramol. Chem.* **18**, 445 (2006).
20. M. Zheng *et al.*, *Science* **302**, 1545 (2003).
21. X. Tu, S. Manohar, A. Jagota, M. Zheng, *Nature* **460**, 250 (2009).
22. S. Wang *et al.*, *Nat. Mater.* **2**, 196 (2003).
23. G. R. Dieckmann *et al.*, *J. Am. Chem. Soc.* **125**, 1770 (2003).
24. A. Ortiz-Acevedo *et al.*, *J. Am. Chem. Soc.* **127**, 9512 (2005).
25. E. Katz, I. Willner, *ChemPhysChem* **5**, 1084 (2004).
26. G. Grigoryan, W. F. DeGrado, *J. Mol. Biol.* **405**, 1079 (2011).
27. Materials and methods are available as supporting material on *Science* Online.
28. G. Ghirlanda, J. D. Lear, N. L. Ogihara, D. Eisenberg, W. F. DeGrado, *J. Mol. Biol.* **319**, 243 (2002).
29. L. A. Capriotti, T. P. Beebe Jr., J. P. Schneider, *J. Am. Chem. Soc.* **129**, 5281 (2007).
30. P. Nygren, M. Lundqvist, K. Broo, B. H. Jonsson, *Nano Lett.* **8**, 1844 (2008).
31. M. J. O'Connell *et al.*, *Science* **297**, 593 (2002).
32. O. N. Torrens, D. E. Milkie, M. Zheng, J. M. Kikkawa, *Nano Lett.* **6**, 2864 (2006).
33. D. Golberg, Y. Bando, C. C. Tang, C. Y. Zhi, *Adv. Mater. (Deerfield Beach Fla.)* **19**, 2413 (2007).
34. A. K. Chakraborty, A. J. Golumbfskie, *Annu. Rev. Phys. Chem.* **52**, 537 (2001).
35. G. E. Crooks, G. Hon, J. M. Chandonia, S. E. Brenner, *Genome Res.* **14**, 1188 (2004).

Acknowledgments: This work was supported by the NSF Materials Research Science and Engineering Center DMR05-20020 grant (to J.M.K., M.D., and W.F.D.), NIH grant no. GM54616 (to W.F.D.), a NSF National Science and Engineering Center grant no. DMR-0425780 (to W.F.D. and M.D.), NSF grant no. DMR-0907226 (to J.M.K.), and NIH grant no. 5F32GM084631-02 (to G.G.). K.A. acknowledges support from the Roy and Diana Vagelos Program in the Molecular Life Sciences, and L.W. acknowledges funding from the NSF–Integrative Graduate Education and Research Traineeship program (grant DGE-0221664). We would like to thank K. A. McAllister for training Y.H.K. in peptide synthesis, and A. E. Keating for comments on the manuscript.

Supporting Online Material
www.sciencemag.org/cgi/content/full/332/6033/1071/DC1
Materials and Methods
Figs. S1 to S15
Tables S1 to S3
References (*26*, *36*–*61*)

8 October 2010; accepted 13 April 2011
10.1126/science.1198841

Impact of Antarctic Circumpolar Current Development on Late Paleogene Ocean Structure

Miriam E. Katz,[1]* Benjamin S. Cramer,[2] J. R. Toggweiler,[3] Gar Esmay,[4] Chengjie Liu,[5] Kenneth G. Miller,[4] Yair Rosenthal,[4,6] Bridget S. Wade,[7] James D. Wright[4]

Global cooling and the development of continental-scale Antarctic glaciation occurred in the late middle Eocene to early Oligocene (~38 to 28 million years ago), accompanied by deep-ocean reorganization attributed to gradual Antarctic Circumpolar Current (ACC) development. Our benthic foraminiferal stable isotope comparisons show that a large $\delta^{13}C$ offset developed between mid-depth (~600 meters) and deep (>1000 meters) western North Atlantic waters in the early Oligocene, indicating the development of intermediate-depth $\delta^{13}C$ and O_2 minima closely linked in the modern ocean to northward incursion of Antarctic Intermediate Water. At the same time, the ocean's coldest waters became restricted to south of the ACC, probably forming a bottom-ocean layer, as in the modern ocean. We show that the modern four-layer ocean structure (surface, intermediate, deep, and bottom waters) developed during the early Oligocene as a consequence of the ACC.

The Antarctic Circumpolar Current (ACC) is a dominant feature of present-day ocean circulation and climate, influencing the strength of meridional overturning circulation, transition depth from surface to deep ocean, gas-exchange rate between atmosphere and deep ocean, and global surface heat distribution (*1*–*4*). Wind-driven ACC upwelling is the major mode of water transport from the ocean interior to the surface, setting the density structure for the ocean interior from the Southern Ocean to high northern latitudes (*5*). The ACC also stabilizes asymmetrical meridional overturning circulation, with more-dense southern-sourced water constrained to bottom depths below the ACC (>2500 m) and overlain by northern-sourced deep waters (Fig. 1).

The ACC "engine" began to develop in the middle Eocene with shallow flow through the Drake Passage between Antarctica and South America (*6*, *7*), followed by rapid deepening of the Tasman gateway between Antarctica and Australia from the late Eocene to early Oligocene (*8*, *9*) and more-gradual deepening of the Drake Passage through the remainder of the Oligocene (*7*) (Fig. 1). It has been proposed that the modern characteristics of the ACC and its effects on deepwater circulation did not develop until the late Oligocene (*9*–*12*). However, a persistent difference in Southern Ocean benthic foraminiferal $\delta^{18}O$ values relative to those of the Pacific and North Atlantic that developed by the early Oligocene did not require a deep ACC; shallow-depth ACC circulation is sufficient for thermal isolation of the high-latitude Southern Ocean from warm surface subtropical gyres (*1*–*4*, *13*), with the potential to affect deepwater source regions. Changes in benthic and planktonic microfossil communities (*14*, *15*), North Atlantic and Pacific drift accumulation (*16*, *17*), and erosional hiatuses in the deep ocean (*18*) support the idea that gradual deep ocean changes occurred through the middle Eocene to late Oligocene.

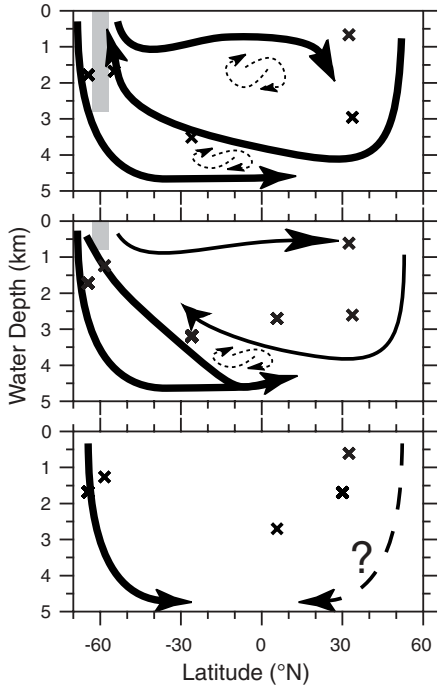

Fig. 1. Effect of progressive ACC deepening on water masses. X's indicate the paleodepths of isotopic records used to reconstruct Eocene-Oligocene water masses in this study. (**Bottom**) No ACC, analogous to pre–mid-Eocene; SCW dominates the deep ocean. (**Middle**) A multilayer ocean begins to develop with a shallow ACC, analogous to the early Oligocene. (**Top**) Multilayer modern ocean with deep ACC, analogous to the late Oligocene to the present.

[1]Department of Earth and Environmental Sciences, Rensselaer Polytechnic Institute, Troy, NY 12180, USA. [2]Theiss Research, Eugene, OR, USA. [3]Geophysical Fluid Dynamics Lab/National Oceanic and Atmospheric Administration, Princeton, NJ, USA. [4]Department of Earth and Planetary Sciences, Rutgers University, Piscataway, NJ 08854, USA. [5]ExxonMobil Exploration, Post Office Box 4778, Houston, TX 77210-4778, USA. [6]Institute of Marine and Coastal Sciences, Rutgers University, New Brunswick, NJ 08901, USA. [7]School of Earth and Environment, University of Leeds, Leeds LS2 9JT, UK.

*To whom correspondence and requests for materials should be addressed. E-mail: katzm@rpi.edu